# Self-Excited Induction Generator Based Microgrid with Supercapacitor Energy Storage to Support the Start-up of Dynamic Loads

Cătălin Petrea ION, Ioan ȘERBAN
*Transilvania University of Brașov, B-dul Eroilor nr. 29, 500036 Brașov, Romania*
*catalin.ion@unitbv.ro*

***Abstract*—A supercapacitor storage system (SCSS) is used for improving the dynamic performances of a microgrid (MG) fed by a self-excited induction generator (SEIG), in the case of the direct start-up of an induction motor (IM) of comparable power. The primary control system contains a voltage source inverter (VSI) with a dump load (DL), to which the SCSS is added. The control strategy for the SCSS consists of injecting power into the VSI DC-link when, because of the overload created by the IM, the DC voltage decreases under the acceptable limit. Thus, the overall performance of the SEIG-supplied MG is significantly improved. Simulations and experimental results accomplished on a laboratory-scale MG validate the effectiveness of the proposed control structure.**

***Index Terms*—microhydro power, generators, induction motors, supercapacitors, DC-DC power converters.**

## I. Introduction

Along with the increased penetration of microgrids (MGs), the major concern is to ensure their stable operation, mainly when operating in autonomous mode. In terms of transient stability, the presence of induction motors (IM) as loads is of significant importance [1], as mainly during faults such an MG can lose its stable operation even if the fault persists only during a typical clearing time [2]. Thus, several studies have been carried out to develop suitable models for analyzing the behavior of MGs supplying dynamic loads [3-7]. In [3], the influence of the IM rotor resistance value on the system performance is highlighted, the authors of [4, 5] have developed small-signal models for medium voltage MGs with dynamic loads, while in [6, 7], the induction motor equations were integrated to form a composite load model for stand-alone MGs.

The IM starting process poses serious technical problems in islanded MGs, as the associated voltage sag and overcurrent may affect the stable operation. The authors of [8] have developed detailed small-signal models for a voltage-source inverter (VSI) MG, which, by using an active compensation technique, is supposed to ensure balancing of the MG. A correlation between the voltage drop and the starting current has been developed in [9], along with a modified control strategy of the photovoltaic-based inverters to improve the MG voltage profile. Other solutions to mitigate this problem rely on a dynamic voltage controller that manages the reactive power sources [10], or on a properly controlled voltage source converter [11]. A hierarchically control microgrid may use fuzzy logic control to mitigate the transients, among which the induction motor start-up [12]. In case of an islanded MG on which five induction motors have to be sequentially started, to ensure the stability, two exciter models for the synchronous generator (SG) have been used [13].

There are many studies that rely on energy storage systems to enhance MGs stable operation during dynamic operating modes. For example, a bank of batteries plus a power converter, under the form of a power coordinating system, is used to support an AC microgrid during faults and induction motors starting [14]. A similar situation is investigated in [15], the difference being that the battery bank is interfaced with the help of a DC-DC converter on the DC side of a PV inverter. The combination between electrochemical batteries and supercapacitors (SCs) is widely used for improving the transient performance of MG and also for reducing the unbalanced power consumption in battery in case of an AC microgrid [16]. This can also be used for smoothing the variations of renewable sources [17]. In a DC microgrid supplied by two small SGs interfaced through uncontrolled rectifiers, the SC substantially contributes to the MG stable operation when pulse loads are supplied [18]. The battery -supercapacitors combination also may ensure the power quality of a MG supplied solely by photovoltaic panels, for both variations of the irradiance and significant load steps [19]. Another MG, presented in [20], is subject to power sharing between two SC units in case of significant load variations, aimed at improving the redundancy and the life of the storage system. SCs alone are used to mitigate the diesel generator start-up in case of a DC microgrid [21], or to reduce load and source transients in a droop-controlled DC microgrid [22].

The research on self-excited induction generators (SEIGs) feeding IMs can be divided into two main areas: without and with regulating power electronics devices. Related to the first category, the study of the autonomous operation of an IG supplying IM has started more than two decades ago [23], focused on ensuring sufficient capacitance to sustain the operation in steady-state and on analyzing the start-up process of different size IMs. The excitation capacitance was computed in order to maintain constant the SEIG output voltage when supplying IMs. The authors of [24] developed a mathematical approach towards predicting the dynamic performance of several parallel connected SEIGs feeding an IM load. An eigenvalue sensitivity analysis for determining the minimum required capacitance for such a topology was

This work was supported by a grant of the Romanian National Authority for Scientific Research and Innovation, CNCS–UEFISCDI, project number PN-II-RU-TE-2014-4-0359.

Digital Object Identifier 10.4316/AECE.2018.02007

the proposed approach.

A comparative study on the influence of long and short-shunt connections on the dynamic performance of an isolated SEIG with a suddenly connected IM has been accomplished in [25]; results have shown that the short-shunt connection ensures a better voltage recovery. In [26], damping resistors across series capacitors were used to attenuate the starting transients of a short-shunt SEIG feeding an IM load. For the short-shunt configuration, the authors of [27] concluded that adding series capacitors ensures a successful IM starting and highlighted the presence of the subsynchronous resonance phenomenon due to large variations in the total load impedance for such a topology.

In [28-30] the behavior of a 2 HP isolated SEIG driven by a small wind turbine and supplying a 0.5 HP IM has been studied. Simulations performed for two IM characteristics (i.e. constant and speed squared torque) have yielded that the constant torque profile causes a large voltage sag, both in terms of voltage drop and duration. Also, the presence of an additional capacitor in parallel with the motor improves the voltage profile and ensures a shorter starting time. A similar topology is investigated in [31], the obtained experimental results showing very large output voltage and frequency variations for different excitation capacitance values and SEIG rotor speeds. An even more dramatic situation is the one investigated in [32], in which a 2.2 kW three-phase SEIG supplies a 1 HP single-phase IM, for self-excitation and phase balancing employing two series connected capacitors and one in parallel with the motor. Successful starting of the motor is achieved only when an additional damping resistance is connected in parallel with the capacitor from the middle phase of the SEIG.

The MG performance issues raised by the IM start-up are well mitigated by using power electronics converters to ensure mainly the voltage balance. In the majority of cases, a transistor-based three-phase inverter is used, named Static Synchronous Compensator (SSC) [33, 34], Static Compensator [35-37] or Voltage and Frequency Controller [38]. Thyristor-based converters are employed, under the form of a Thyristor Controller Reactor [39] or a Static VAR Compensator [40]. Finally, an Electronic Load Controller consisting in a diode rectifier in series with a chopper and a dump load (DL) may be used to balance the system under dynamic load, this solution being the most efficient in terms of power quality, control flexibility and power density [41].

With respect to the literature, the transient process during by the IM start-up is usually assessed by simulations. The ratio between the IM power and the MG total power varies within wide limits. In [10], the start-up of a 100 kVA IM connected to an MG supplied by a 1 MVA synchronous generator and two 0.75 MVA wind turbines is investigated. The start-up of an IM whose power is half the converter power that supplies the MG is investigated through simulations in [11]. Experiments were accomplished in [8], where a small power IM start-up will produce the VSI tripping in normal operation, while the activation of a voltage-reference-based compensator will limit the voltage sag to 7.5% for about 0.6 s. A 1.1 kW IM is started on an 80 kVA MG in [12], while in [13] 5 IMs rated from 450 HP to 1000 HP are sequentially started on a 7000 HP MG.

In case of SEIGs based MGs, the transient process during the IM start-up is experimentally assessed only in two papers. In [35] the IM/IG power ratio is 20%. For an IM/IG ratio of 50%, a star-delta starting topology is used to limit three times the starting currents [38].

The relevance of the present work can be revealed by the need of investigating the MG performance in a more restrictive situation than the ones mentioned so far, more precisely when the power of the IM to be started is comparable with the MG one. In this case, for an MG supplied solely by a self-excited induction generator, an IM/SEIG active power ratio of 4/5 is considered. The main contribution of this study consists in enhancing the dynamic behavior during the IM direct-on-line start-up by adding to the MG control structure a short-term energy storage based on a SC deployed only during transient processes. As shown by both simulation and experimental results, in comparison with the conventional control method, the proposed solution allows a significant reduction of the voltage sag during the severe transient processes, for this high IM/SEIG ratio.

After the Introduction, the paper is organized as follows: Chapter II details the studied MG configuration and its control, the simulation and experimental results are presented in Chapter III, Chapter IV discusses the obtained results with respect to other similar studies while Chapter V presents the main paper conclusions.

## II. MG Configuration and Control

### *A. MG Configuration*

The studied MG relies on a squirrel-cage induction generator driven by a hydraulic turbine, excited by a capacitor bank ($C_{exc}$) and supplying static and dynamic loads, as shown in Fig. 1.

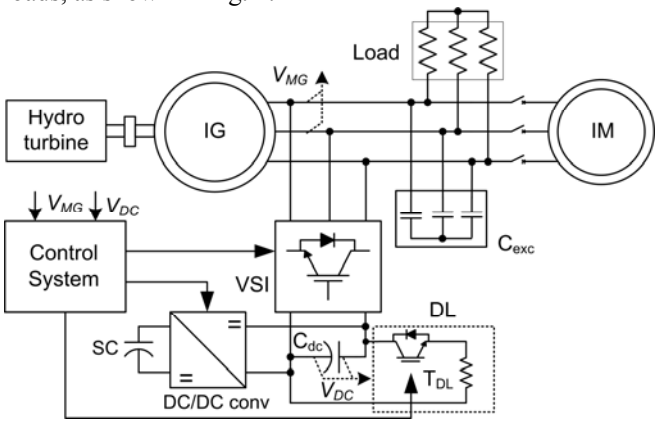


Figure 1. SEIG-based MG structure

For voltage and frequency control, a VSI, interfaced through a high-voltage DC link ($C_{dc}$) with a DL circuit is used. The DL is actually a resistor supplied trough a PWM controlled DC chopper. An *LC* filter ensures the VSI connection to the SEIG terminals. To improve the dynamic behavior during transients, a Super Capacitor Storage System (SCSS) was interfaced with the VSI DC-link through a bidirectional DC-DC converter. An uncontrolled micro hydro turbine was chosen; thus, considering that the output power of the generator is constant, the DL is used to manage the exceeding active power. At the IM direct starting a dynamic process occurs. The IM load is

considered of constant torque type.

Excepting the generator start-up process, during which a controlled driving algorithm is implemented [42], the VSI operates with a fixed frequency reference, thus keeping the MG frequency constant. To keep the voltage at the rated value, the DL is controlled to dissipate the exceeding active power of the MG (actually the difference between the power produced by the IG and the one requested by the load). In order to support the MG during severe transients, the SCSS is controlled to inject power into the VSI DC-link during overloads when the DC-link voltage ($V_{DC}$) decreases under a minimum threshold (as will be presented in Section C).

### *B. Voltage and Frequency Control*

The DL and VSI control systems are presented in Fig. 2. For voltage regulation, two proportional-integrative (PI) controllers are employed, as illustrated in Fig. 2a.

The first one ($PI_1$) is the leading voltage regulator and is used to compensate the voltage drops across the inverter arms and filter, IG leakage impedances, and elements that contribute to the MG voltage decrease. The MG RMS line voltage ($V_{MG}$) represents the feedback signal, being compared with a 400 V reference signal ($V_{MG}$*).

The resulting error serves as input to the first PI controller, which gives the reference for the DC-link voltage ($V_{DC}$*), which is transmitted to the next controller. The second PI (i.e. $PI_2$) maintains constant the voltage across the $C_{dc}$ capacitor by controlling the power dissipated on DL. The measured DC voltage ($V_{DC}$) is compared with the reference one ($V_{DC}$*), and the resulting error is fed to $PI_2$ controller, which outputs the duty cycle of the PWM signal that controls the power dissipated on DL.

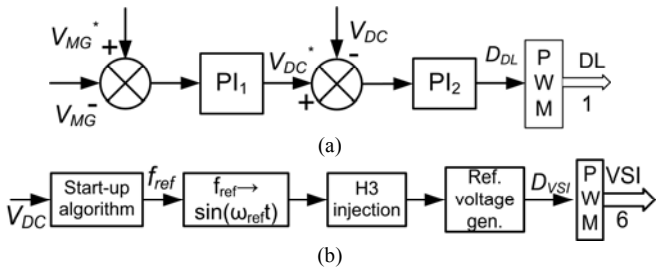


Figure 2. The voltage and frequency control system: a) DL control, b) VSI control

The VSI control loop, depicted in Fig. 2b, generates the control signals for the six VSI power transistors. As input signal it has the measured DC voltage ($V_{DC}$), because it also has to handle the start-up process, which is initialized by a local energy source placed on the DC link in the form of either a low-voltage DC source, or by the SCSS pre-charged from a previous operation (this case is reserved for future studies). The start-up algorithm provides the reference frequency $f_{ref}$, which, after the IG speed and the VSI DC voltage reach the rated values, is set to 50 Hz where it remains during the IG normal operation. Details about the start-up process are presented in [42] and, therefore, not included in the current paper. However, an important remark is that during severe dynamic events (e.g., significant loads variations), the dramatic decrease of the DC-link voltage can trigger the start-up algorithm. Consequently, as revealed by the simulation and experimental results presented in Ch. III, the reference frequency $f_{ref}$ is automatically modified according to the DC link voltage sag. Note that the effect is rather helpful for the recovering of the MG parameters after an overload, as forcing the frequency to decrease will boost the power production of droop-controlled generators, in the case of multi-units MGs [43]. Moreover, due to the natural response of the hydro turbine-generator system, the reduction of the MG frequency causes the decreasing of the IG speed depending on the machine slip and loading, which releases a certain amount of power available for the IG due to the high inertia of the mechanical aggregate. Therefore, by using the same mechanism, the proposed control solution ensures both the IG starting-up and the frequency support during severe dynamic events.

### *C. SC Control*

Fig. 3 shows the connection scheme of the SCSS to the VSI, where a non-isolated bidirectional DC-DC converter is used to transfer the power between the SC and DC-link. For the purpose of this paper, the SC is modelled as a simple *RC* network, with $C_{sc}$ being the rated capacitance and $r_{sc}$ the rated equivalent series resistance [44].

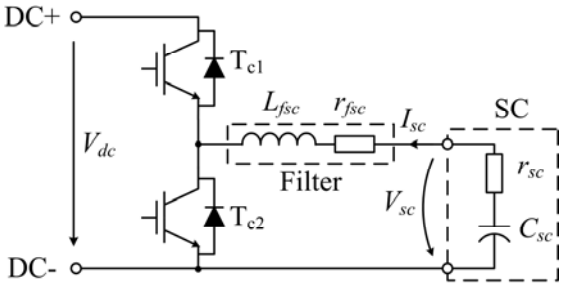


Figure 3. Connection scheme of the SC to the VSI DC-link

Fig. 4 presents the control diagram of the SCSS based on a cascaded current-voltage topology. The inner current controller includes a PI structure with a voltage feed-forward loop, as shown in Fig. 4a, providing at the output the duty cycle $D_c$ of the PWM signals for the two transistors $T_{c1}$ and $T_{c2}$ shown in Fig. 3. The SC current reference ($I_{sc}^*$) is provided by a DC voltage controller ($PI_3$), which operates as described in the following.

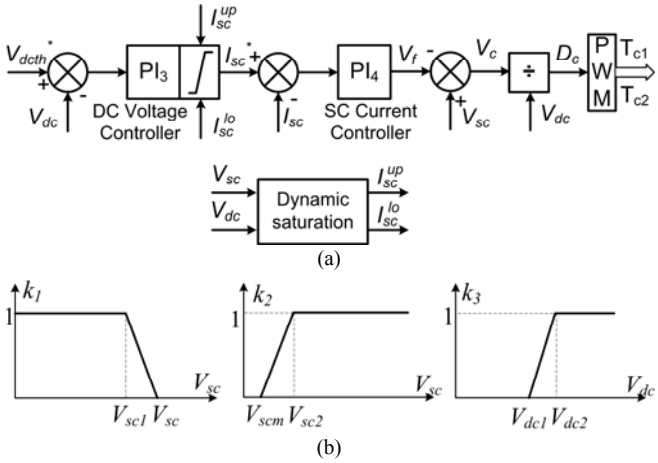


Figure 4. Control diagram of the SC converter: a) SC control; b) Limitation coefficients of SC current reference

The main purpose of the SC is to provide support during severe dynamic events that can lead to large voltage sags in the MG, as the simulation and experimental results will show. Therefore, the SCSS is controlled to inject power into

the VSI DC-link only when $V_{dc}$ decreases under a certain value. For this purpose, the voltage controller shown in Fig. 4a is configured to maintain the DC-link voltage to a preset threshold value ($V_{dcth}^{*}$), therefore maintaining the VSI capability to regulate the MG voltage, as described in Section B. The control scheme also includes a mechanism to ensure the SC charging during the periods in which the VSI operates in normal conditions (i.e. the VSI input power is high enough to maintain a stable DC-link voltage) and also to limit the charging/discharging current when the SC voltage reaches the maximum/minimum value.

The voltage controller includes a dynamic saturation at the output that limits the reference current $I_{sc}^{*}$ to the upper and lower extremities $I_{sc}^{up}$ and $I_{sc}^{lo}$, respectively, which are defined according to the SC maximum current ($I_{scM}$) as follows:

$$I_{sc}^{lo} = I_{scM} \cdot k_1 \cdot k_2 \tag{1}$$

$$I_{sc}^{up} = I_{scM} \cdot k_2 \tag{2}$$

The saturation limits are calculated by using three subunit coefficients (i.e. $k_1$, $k_2$ and $k_3$), which depend on the SC and DC-link voltages according to the diagrams presented in Fig. 4b. The first two coefficients are used to limit the charging and discharging current when the SC voltage reaches a maximum ($V_{scM}$) or minimum ($V_{scm}$) value. In order to reduce the transients associated with the sudden decreasing of the SC charging/discharging current, the limitation is accomplished gradually starting from safe voltage thresholds ($V_{sc1}$ for $k_1$ and $V_{sc2}$ for $k_2$). The maximum SC voltage is considered equal to the SC rated voltage $V_{scM}$=$V_{scr}$, while the minimum SC voltage $V_{scm}$ mainly depends on the converter capabilities in terms of rated current and minimum duty cycle. Thus, the SC state-of-charge (*SOC*) is maintained within normal operating limits, where *SOC* (expressed in p.u.) is calculated from the SC voltage and current by means of the following expression:

$$SOC(t) = SOC(t - \Delta T) - \frac{V_{sc} \cdot I_{sc}}{E_{sc,r}} \cdot \Delta T \tag{3}$$

where: $\Delta T$ is the state-of-charge control sampling time; $V_{sc}$, $I_{sc}$ are the measured SC voltage and current, respectively; $E_{sc,r}$ is the rated SC energy.

The SC charging process starts only when the VSI maintains a minimum DC-link voltage ($V_{dc1}$) corresponding to the operating case with an excess of power absorbed by the VSI. Therefore, the charging current limit ($I_{sc}^{lo}$) is modified according to the DC-link voltage by means of the coefficient $k_3$, as shown in Fig. 4b, where for the studied case $V_{dc1}$=600 V and $V_{dc2}$=650 V.

### *D. Sizing the Supercapacitor*

The SC is sized according to the requirements of the proposed application and taking into account the practical limitations of commercially available SCs and bidirectional power converter. As mentioned previously, the SC is integrated within the SEIG control system to provide power support by injecting a certain amount of power to the VSI's DC-link during overloads produced by an IM start-up. Therefore, the SC system operates with an equivalent constant-power load, where the parameters of the power pulse (i.e. magnitude $P_p$ and duration $T_p$) were extracted from experimental measurements. The SC calculation implies determining the number of required cells mounted in series, several methods being addressed in literature mainly for electric vehicles and for microgrids [45-47]. Of these, the calculation procedure provided in [45] was found to match best the specific requirements of this application.

Considering an ideal capacitor model (i.e. without equivalent series resistance), the minimum number of SC cells required to deliver the constant power $P_p$ over the time period $T_p$ can be calculated as follows [45]:

$$n = P_p / V_{cell}^2 \left( \frac{T_p}{C_{cell}} + \sqrt{\frac{T_p^2}{C_{cell}^2} + \frac{V_{cell}^2}{I_{\max}^2}} \right) \tag{4}$$

where: $C_{cell}$, $V_{cell}$ are the capacitance and voltage of a single cell, respectively, and $I_{max}$ is the maximum SC current.

Depending on the used SC cell type, the two parameters $C_{cell}$, $V_{cell}$ are known. Moreover, in order to increase the SC pack lifetime, the cell should operate at a slightly lower voltage than the rated value. Therefore, by considering the steady-state value of the SC state-of-charge ($SOC_0$), the cell voltage has to be corrected as follows (with $SOC_0$ expressed in per unit):

$$V_{cell}^{'} = V_{cell} \sqrt{SOC_0} \tag{5}$$

The maximum current $I_{max}$ is mainly determined by the current limit of the power converter that interfaces the SC with the VSI DC-link, as shown in Fig. 3. A higher value of $I_{max}$ implies that the SC has to deliver more power in short periods of time and, therefore, a better utilization of the SC capacity is achieved. However, the power electronics would have to be oversized in order to carry the higher SC current. Therefore, the optimal value of $I_{max}$ involves a tradeoff between the size of the power converter and the SC capacitance. For the application proposed in this paper, the voltage and current ratings of the bidirectional converter and VSI are considered similar; hence the IGBTs used in the experimental setup will provide $I_{max}$ as the current limit.

In applications with a relatively low current, the voltage drop of the SC's equivalent series resistance can be neglected and (4) provides a good approximation of the number of cells. However, when high currents are involved, as in the case of the application presented in this paper, the effect of SC's equivalent resistance has to be taken into account. Therefore, as detailed in [45], considering the cell's series resistance ($r_{cell}$) the minimum number of cells required to deliver the power pulse $P_p$ in the time period $T_p$, results as solution of the following equations system:

$$\frac{\mathrm{d}V_{sc}}{\mathrm{d}t} = -V_{sc} + \frac{\sqrt{V_{sc}^2 - 4r_{sc}P_p}}{2r_{sc}C_{sc}} \tag{6}$$

$$V_{sc} = n \cdot V_{cell} \tag{7}$$

$$r_{sc} = n \cdot r_{cell} \tag{8}$$

$$C_{sc} = \frac{C_{cell}}{n} \tag{9}$$

To make sense, the part under square root of (6) must be positive and, therefore, the following condition must be met when selecting the SC cell:

$$V_{sc} \geq 2\sqrt{r_{sc}P_p} \tag{10}$$

After solving (3) by a numerical method, the time variation of SC current ( $I_{sc}$ ) results as:

$$I_{sc}(t) = \frac{V_{sc}(t) - \sqrt{V_{sc}^2(t) - 4r_{sc}P_p}}{2r_{sc}} \tag{11}$$

Since the power must remain constant, the current will reach the maximum value at the end of the discharge time, when the voltage $V_{sc}$ is at minimum and, therefore, the current $I_{max}$ results from (11) for $t = T_p$. In order to limit the maximum current according to the IGBTs specifications, as previously mentioned, the minimum number of cells is calculated from (6)-(10) by means of an iterative algorithm, which increments n until the current condition $I_{sc}(T_p) \leq I_m$ is fulfilled.

Based on the above procedure, the SC pack was sized using a certain class of cells from the manufacturer [48], with the following specifications: $C_{cell}$ = 100 F, $V_{cell}$=2.7 V, $r_{cell}$=15 mΩ. The IGBTs of the bidirectional converter are sized to $I_{max}$=40 A. The power pulse parameters ($P_p$ and $T_p$) to support the VSI during the direct start-up of the considered IM have been determined according to $P_p$=5 kW and $T_p$=0.1 s, for simulations and also for experiments. Applying the above-described SC sizing algorithm, the minimum number of cells results as $n$=63. Therefore, for simulations, an SC pack with the equivalent capacitance of $C_{sc}$=1.6 F and the equivalent series resistance of $r_{sc}$=0.94 Ω is considered.

## III. Simulation and Experimental Results

The proposed MG support during transients is investigated by means of computer simulations and experimental results. The simulations were accomplished in MATLAB/Simulink, while a laboratory test-bench, shown in Fig. 5 (block diagram) and Fig. 6 (illustration), was used for experiments. For consistency, the MG parameters, listed in Appendix A, were the same in simulations and experiments.

The real-time control and data acquisition were implemented with the help of a dSPACE DS1103 board. The experimental results were acquired numerically using a graphical user interface developed in ControlDesk. The voltages and currents were measured using precision Hall-effect transducers (LV25P for voltages and LA55P for currents), while the integrated 16-bit analog-to-digital converters of the dSPACE DS1103 board provided high-accuracy signals to the control scheme. The frequency was measured by means of a three-phase phase-locked-loop (PLL), based on a synchronous reference frame transformation and amplitude normalization of the input voltages [49]. The RMS voltage was calculated using a standard block from Matlab/SimPowerSystem library, based on a running average window of one cycle of the fundamental frequency (i.e. 50 Hz) [50].

In order to mimic the behavior of the primary energy source, a micro-hydro turbine emulator was used. It consists in a 7.5 kW induction motor (IM*), mechanically coupled with a 3.3 kW IG through a torque transducer, and supplied by a frequency converter.

The operation of the micro hydro turbine emulator relies on a control loop in which the input parameter is the (IM*) electromagnetic torque ($T_m$), while the output parameter is the motor reference speed ($\Omega_{ref}$), which is provided by the dSPACE DS1103 interface through a digital to analogue (DAC) port. By imposing the (IM*) rotational speed, the motor-generator system is controlled to follow the mechanical characteristic of a micro-hydro turbine. Details about the start-up process are presented in [42] and, therefore, not included in the current paper.

The IM is rated at 2.2 kW and its load is emulated by using a 2.2 kW induction generator (IG*), which is mechanically coupled with the IM as shown in Fig. 5. IG* is excited by a 40 μF capacitor bank and supplies a three-phase balanced resistive load. The behavior of the SCSS system is replicated with the help of a voltage-controlled DC power source, which is connected on the VSI DC-link as shown in Fig. 5. The reference voltage for the DC power source is set to the threshold voltage $V_{dcth}^*$=580 V. Therefore, when $V_{dc}$ decreases under this value the DC source starts regulating the DC-link voltage similar to the SCSS system operation, as presented in Section C.

Both simulations and experimental evaluations focus on two scenarios of interest to evaluate the dynamic load influence on the MG performance:

Scenario 1) IM direct start-up on the initially loaded MG, with and without support;

Scenario 2) IM direct start-up and subsequent loading on an initially non-loaded MG, with and without support.

To assess the MG behavior during the above-mentioned situations, the simulation results and measurements for each experiment were used to calculate the following dynamic performance indices (where $V_{MG}$ and $f_{MG}$ are the line-to-line voltage and the frequency of MG, respectively):

- voltage deviation ($\Delta V$) and frequency deviation ($\Delta f$), expressed by (12) and (13);
- voltage settling time ($t_{sV}$), calculated as the time required to settle the voltage within the ±4 V band around $V_0$ = 400 V;
- frequency settling time ($t_{sf}$), calculated as the time required to settle the frequency within the ±50 mHz band around $f_0$ = 50 Hz;

$$\Delta V[\%] = \left(1 - \frac{V_{MG}}{V_0}\right) * 100 \tag{12}$$

$$\Delta f[\%] = \left(1 - \frac{f_{MG}}{f_0}\right) * 100 \tag{13}$$

Both simulation and experimental results are concentrated in Table I.

### A. Simulation Results

Simulations were performed to test the effectiveness of the SCSS in supporting the MG during severe transients.

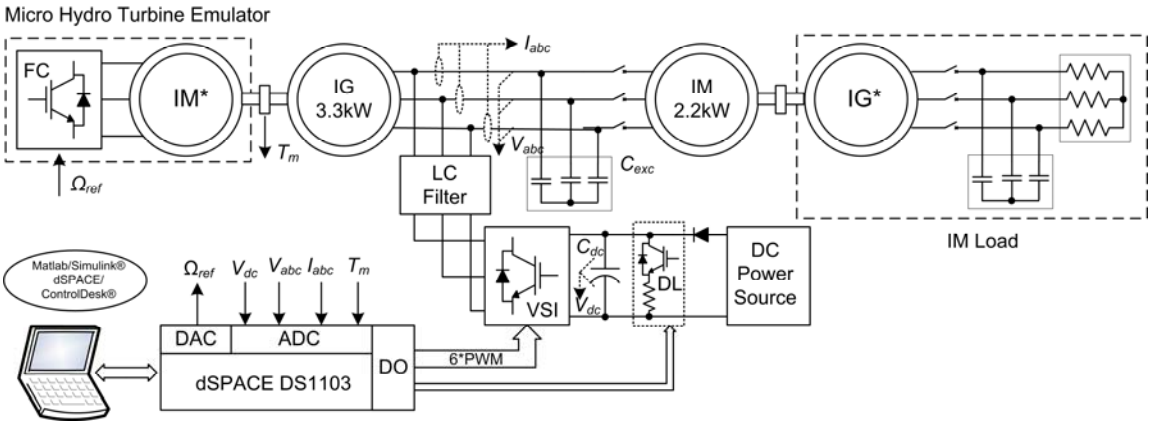


Figure 5. Block diagram of the laboratory MG

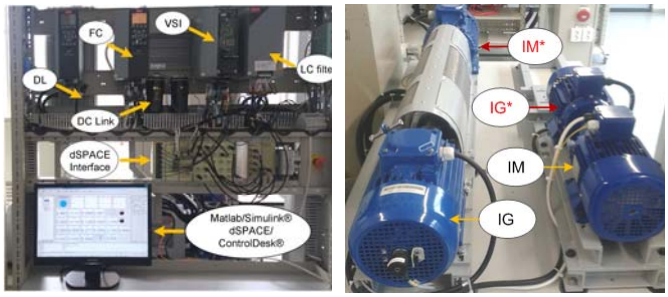


a) b)

Figure 6. MG laboratory illustration: a) control part, b) electromechanical part

TABLE I. EVALUATION OF POWER QUALITY PARAMETERS

| MG Loading [%] | $\Delta V$ [%] | | | | $t_{sV}$ [s] | | | | $\Delta f$ [%] | | | | $t_{sf}$ [s] | | | |
|---|---|---|---|---|---|---|---|---|---|---|---|---|---|---|---|---|
| | Without support | | With support | | Without support | | With support | | Without support | | With support | | Without support | | With support | |
| | S | E | S | E | S | E | S | E | S | E | S | E | S | E | S | E |
| $C_{1.1}$ | 32.5 | 21.6 | 17.0 | 18.0 | 0.6 | 0.5 | 0.4 | 0.4 | 14.8 | 10.7 | 1.6 | 2.5 | 0.2 | 0.3 | 0.2 | 0.3 |
| $C_{1.2}$ | 34.5 | 34.1 | 18.3 | 17.8 | 0.7 | 0.8 | 0.5 | 0.4 | 16.4 | 20.4 | 2.6 | 3.0 | 0.3 | 0.5 | 0.2 | 0.2 |
| $C_{1.3}$ | 35.5 | 34.8 | 19.8 | 18.6 | 0.8 | 1.2 | 0.6 | 0.4 | 18.3 | 24.4 | 3.8 | 3.4 | 0.3 | 0.9 | 0.2 | 0.2 |
| $C_2$ | 29.8 | 36.3 | 15.8 | 17.1 | 0.5 | 0.9 | 0.3 | 0.4 | 14.0 | 18.0 | 1.6 | 2.6 | 0.2 | 0.3 | 0.2 | 0.2 |

Note: S and E stand for simulation and for experiment, respectively.

Thus, for the first scenario, (IM was started-up, at $t$=1.3 s), the MG supplied an initial three-phase balanced resistive load of three values: $C_{1.1}$=0%, $C_{1.2}$=25% and $C_{1.3}$=50% of the IG nominal power, respectively, the SCSS being initially disabled.

The performance indices, listed in the first three rows of Table I, tended to worsen as the initial load ratio increases, both in terms of voltage and frequency deviation. More precisely, the voltage deviation varies from $\Delta V$=32.5%, when there is no initial load, to $\Delta V$=35.5% when the load is 50% of the total available power. The same tendency persists when the SCSS is enabled, but the voltage sag is reduced to almost half, as well as the voltage settling time ($t_{sV}$), which is in the range of 0.4-0.6 s. As for the MG frequency and implicitly for the IG rotor speed variation, the simulations demonstrate a similar trend, as without support the frequency deviation varies from $\Delta f$=14.8%, at no load to $\Delta f$=18.3%, at 50% load, while the frequency settling time is $t_{sf}$=0.3 s. When the SCSS is enabled, the frequency sag is reduced 6 times, while the frequency settling time becomes $t_{sf}$=0.2 s.

Figs. 7 and 8 present the variations of the line voltage and frequency of the MG, respectively, for all investigated situations. As one can see, while without support the initial MG loading has a visible effect on the voltage recovery behavior, enabling the SCSS support leads to a substantial improvement in terms of both voltage variation and voltage load dependence.

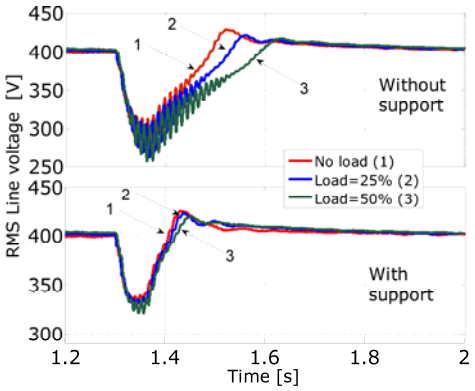


Figure 7. Voltage variation for scenario 1

Next, when the IM is started at no-load and then loaded (scenario 2), the SCSS action reduces the voltage deviation from $\Delta V$=29.8% to $\Delta V$=15.8% and the voltage settling time from $t_{sV}$=0.5 s to $t_{sV}$=0.3 s.

The frequency deviation is reduced from $\Delta f$ =14% to $\Delta f$ =1.6%. The MG line voltage and frequency variation are depicted in Fig. 9, while Fig. 10 shows the DC voltage and generator speed variations. It can be noticed that the DC voltage sag is reduced 2.5 times by the SCSS action. Also, the IG rotor speed (initially at around 1555 rpm) decreased 5 times less when the SCSS was enabled, as shown in Fig. 10.

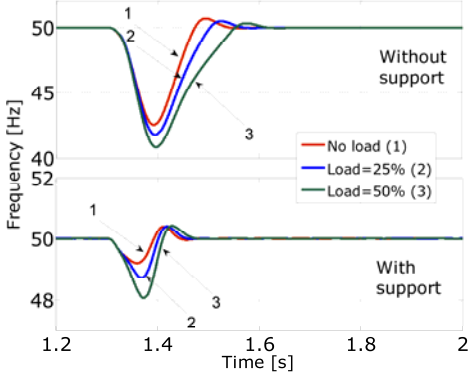


Figure 8. Frequency variation for scenario1

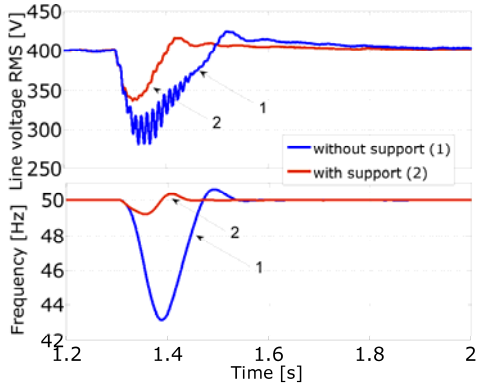


Figure 9. Voltage and frequency variation for scenario 2

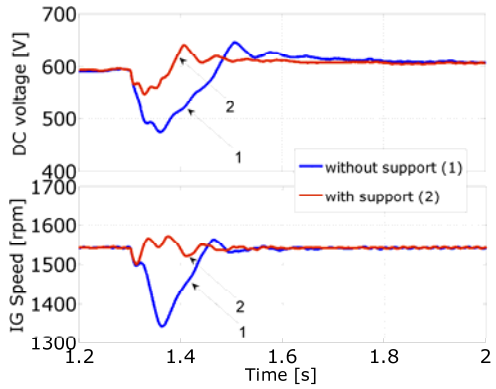


Figure 10. DC Voltage and SEIG rotor speed variation for scenario 2

Figs. 11 and 12 show the simulation results on the SC side, for the worst case (when the initial MG load is 50% of the nominal one). It can be observed that the SC injects power for approximately 0.09 s, during the overload created by the IM load connection. Within this interval, the voltage decreases from the initial value of 160 V to 121 V, while the injected maximum current is $I_{max}$=39 A, as results from Fig. 11. The SC power has a peak of around 4.7 kW, yielding an injected energy of 423 Ws. The SC state-of-charge decreases from the initial value of SOC=90% to SOC= 88.2%, as can be seen in Fig. 12. Right after the end of the transitory regime the SC slowly begins to charge from the VSI DC-link, as there is excess of power in the MG. After the upper SOC value is reached, according to the description from Section B of Chapter II, the SCSS remains connected without exchanging power with the VSI until a new event triggers the support of the DC-link voltage. One should observe that the SOC has an insignificant change of only 2%, which means that a smaller capacitance could be used. However, as also highlighted in Section D of Chapter II, the SC selection was based on several practical criteria. Moreover, other features requiring higher SC's energy usage can be ensured by the proposed system, as detailed in [51].

### *B. Experimental Results*

Experiments were performed for the two above-mentioned scenarios, replicating the simulations and the main results are included in Figs. 13 and 14. For the first scenario, represented in Fig. 13, it can be seen that, since the initial MG load is higher, the IM starting process has more impact on the MG power quality. Thus, the voltage deviation increases from a value of $\Delta V$=21.6% for no-load to $\Delta V$=34.8% for half load. The SCSS support reduces this variation to around $\Delta V$=18%, which is less than for the solution reported in [36], where a star-delta starting topology is employed. A more significant improvement is registered for the voltage settling time, which is reduced for a 50% load from $t_{sV}$=1.2 s to $t_{sV}$=0.4 s.

Regarding the frequency variation, it should be mentioned that while in simulations the inertia of the hydro-turbine could be modeled accurately, in the case of experiments the limited reaction time of the driving system part of the hydro turbine emulator did not allow to replicate the dynamic behavior of the mechanical system with a similar precision as in simulations. The effect is that the IG rotor speed has a larger variation during transients, leading to more significant frequency variations than in simulations. Thus, without support, the frequency variation increases from $\Delta f$=10.7% at no load to $\Delta f$=24.4%, for 50% load, and the frequency settling time varies from $t_{sf}$=0.3 s to $t_{sf}$=0.9 s. Note that, for the worst case scenario, the frequency drops to 39 Hz, which in a real MG would trigger the under-frequency protection, but to be able to clearly quantify the influence of the IM direct starting on such an MG, this protection mechanism was not considered in the experiments nor in simulations. When the SCSS is enabled, the frequency deviation and settling time were kept around $\Delta f$=3% and $t_{sf}$=0.2 s respectively. Fig. 13 also shows the variations for the DC voltage, IG active and reactive power circulations, without and with the SCSS.

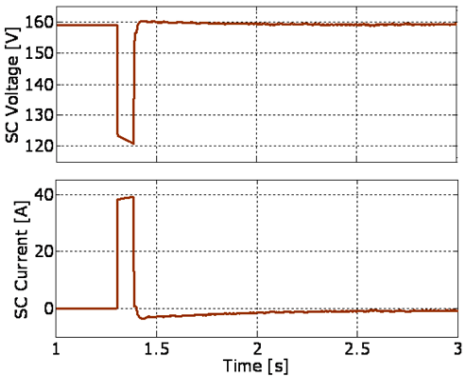


Figure 11. Simulation results for SC: voltage and current variation

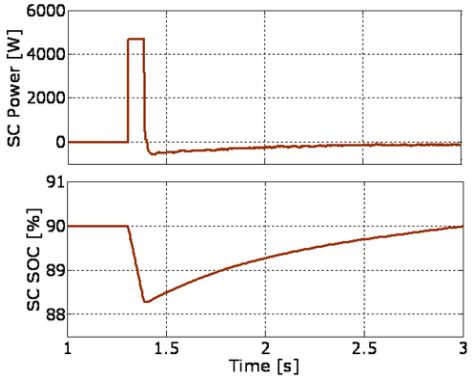


Figure 12. Simulation results for SC: power and SOC variation

Next, the IM starting and loading was experimentally assessed. Before the IM connection, the IG was delivering its nominal output power (i.e. 3.3 kW), at the rated nominal speed of 1555 rpm and no load was connected to the MG. At $t$=0.1 s, the IM is suddenly connected and loaded, reaching its steady-state at $t$=1.5 s. The IM absorbed active power is around 2 kW while the required reactive one 1.7 kVAr. The captured waveforms are shown in Fig. 14 (left side).

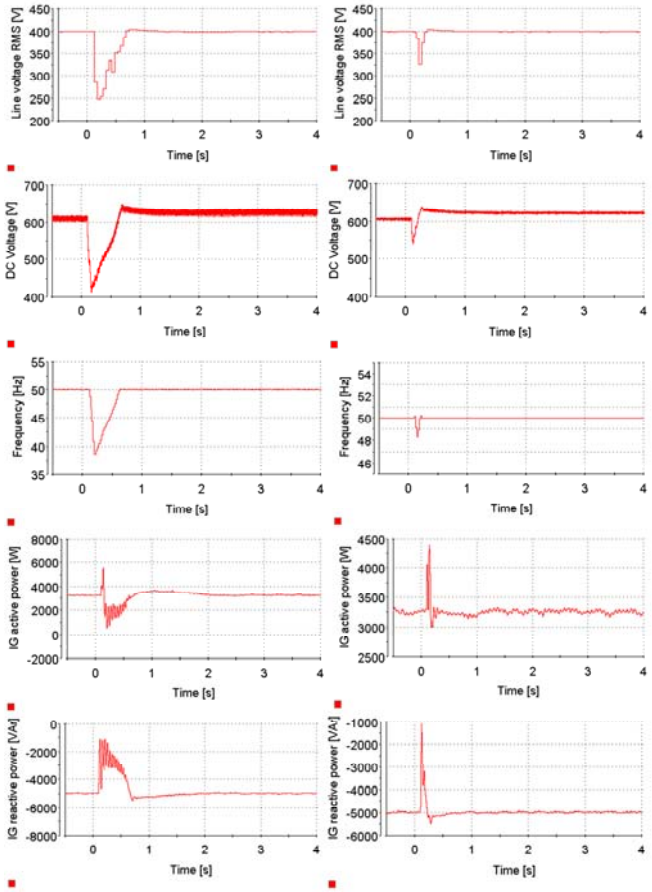


Figure 13. Experimental results for scenario 1 (50% load): without (left) and with support (right)

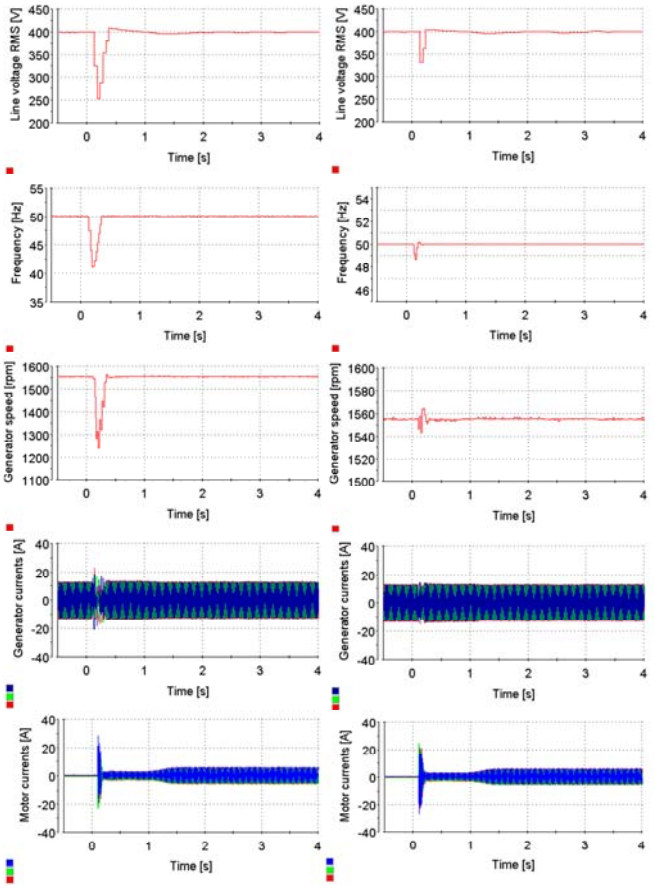


Figure 14. Experimental results for scenario 2: without (left) and with support (right)

The MG voltage decreases significantly at the moment the IM is connected, up to 255 V, which represents a voltage sag of around $\Delta V$=36%. It returns within the assumed settling time in almost $t_{sV}$=1 s. The frequency also decreases to around 41 Hz, and the generator speed drops to 1250 rpm, but in this case the frequency settling time is under $t_{sf}$=0.3 s. For the same initial conditions and with the SCSS enabled, the system performance is significantly improved. Thus, the voltage drop is reduced to $\Delta V$=17% and the corresponding settling time to less than half ($t_{sV}$=0.4 s). On the frequency side, the decrease is limited to only $\Delta f$=2.6% of its nominal value and the settling time reduced by 27%. The generator speed varies insignificantly, as shown in Fig. 14 (right side). One thing to be noticed is the IG currents variation at the moment of the IM connection, which decrease for a very short period of time to a minimum value of 5.8 A, from a steady-state value of 9.5 A.

## IV. Discussion

The major improvement achieved by the use of SCSS during the IM direct starting on an isolated MG supplied by a SEIG and with an IM/SEIG ratio of 4/5 is the significant reduction of the associated voltage sag to $\Delta V$=18% for no longer than $t_{sV}$=0.4 s. As for the voltage sag influence on sensitive consumers like personal computers, the obtained voltage profile is within the ITIC and SEMI F47 power acceptability curves, as stated in [52]. Moreover, the frequency variation is kept under $\Delta f$=3.5% and its recovery time under $t_{sf}$=0.2 s.

Compared to other references, the results obtained through the proposed method and presented in this paper show significant improvements mainly on the voltage side where the induced sag is relatively small for such a high IM/SEIG ratio. For example, in [9] the voltage drop associated with the IM start-up varies from $\Delta V$=20% to $\Delta V$=60%, while the starting currents vary from 7.2 A to 18.74 A. Likewise, a voltage drop $\Delta V$=23% for an IM with a rated power of only 4% from the power delivered by the sources that supply the MG is reported in [10].

For an IM with half the power of the converter that supplies the MG a voltage drop $\Delta V$=25% for a period of 3 s is registered in [11]. Another study presented in [8] shows that for an MG supplied by a 1 kVA VSI, a very small power IM start-up will produce the VSI tripping in normal operation, while the activation of a voltage-reference-based compensator will limit the voltage sag $\Delta V$=7.5% for about 0.6 s. In [12], a 1.1 kW IM start-up will induce a $\Delta V$=18%, but the total power of the MG is 80 kVA.

A lower voltage sag $\Delta V$=12% is reported in [13], but the IM/generator ratio is only 1/7. In case of SEIGs-based MGs, for an IM/IG power ratio of 20%, at the moment of the IM connection the IG currents variation is almost twice the nominal value and the proposed control topology ensured that the IG voltage does not collapse [35].

For an IM/IG ratio of 50%, a star-delta starting topology is used in [41] to limit three times the starting currents, and recording a voltage sag $\Delta V$=25%. An important point worth noting is that with the solution proposed in the present paper, the SEIG currents decreased at the moment the IM was directly started to 61% from their nominal value,

significantly smaller compared to 33% reported in the reference mentioned above.

Moreover, compared with other topologies that employ battery-based energy storage systems to mitigate the effects of the induction motor direct starting, the obtained results show better performance. For a 9% IM/MG power ratio, a voltage sag $\Delta V$=26% is measured at the IM start-up in [14]. For a lower IM/IG ration (i.e. 6%) the voltage sag obtained in [15] is smaller ($\Delta V$=18%), but at the expense of a longer settling time ($t_{sV}$=1 s) [15]. In the case of a SEIG-based MG with a 40% IM/IG ratio [34], the IM starting produces a voltage sag $\Delta V$=40% for almost 0.7 s.

Table II shows a comparison of the obtained results in terms of voltage sag amplitude and duration with similar studies that deal with induction motor starting in microgrids.

TABLE II. RESULTS COMPARISON

| No. | IM/MG ratio [%] | Starting method | $\Delta V$ [%] | $t_{sV}$ [s] | Reference |
|---|---|---|---|---|---|
| 1 | 50 | Direct | 25 | 3 | [11] |
| 2 | 4 | Direct | 18 | 0.2 | [12] |
| 3 | 25 | Direct | 25 | 0.12 | [35] |
| 4 | 50 | Star-delta | 20 | 1 | [41] |
| 5 | 40 | Direct | 40 | 0.7 | [34] |
| 6 | 9 | Direct | 26 | 0.16 | [14] |
| 7 | 6 | Direct | 18 | 1 | [15] |
| 8 | 83 | Direct | 18 | 0.4 | this paper |

Note: Positions 5-8 use storage elements

## V. CONCLUSIONS

A dynamic support method for an autonomous microgrid (MG) based on a self-excited induction generator (SEIG) when supplying a directly-connected induction motor (IM) of comparable power (i.e. IM/IG power ratio is 4/5) was presented in the current paper.

The main contribution of the paper consists of using a supercapacitor storage system (SCSS) for improving the dynamic performances of a MG fed by a SEIG, in case of IM start-up ad loading. The proposed control solution has been validated through simulations and experimental investigations on a laboratory-scale MG, for two representative scenarios (i.e. the IM start-up when the MG supplies an initial load and the IM start-up and loading). The results focused on the improvement of IG performance when using the SCSS.

Four performance indices (i.e. voltage deviation and settling time, frequency deviation and settling time) were used to quantitatively assess the SCSS support.

Compared with similar approaches presented in literature, dealing with the transients introduced by an IM starting in a SEIG-based MG and validated through experimental tests, the proposed control topology (having a very high IM/IG power ratio, too), brings the following improvements: reduction of the voltage sag under 20%, even though direct starting is employed - also the voltage recovery time is kept under 0.4 s; reduction of the frequency sag under 3.5% - also the frequency recovery time is kept under 0.2 s; significant reduction of the MG currents oscillations at IM starting.

## APPENDIX A - MG PARAMETERS

| | Element | Parameters | Values |
|---|---|---|---|
| Hardware | IG | Rated (output) power | 3.3 kW |
| | | Nominal voltage | 400 V |
| | | Nominal current | 8.64 A |
| | | Pole pairs number | 2 |
| | IM | Rated electrical power | 2.75 kW |
| | | Rated (mechanical) power | 2.2 kW |
| | | Nominal voltage | 400 V |
| | | Nominal current | 5 A |
| | | Pole pairs number | 2 |
| | VSI | Rated power | 9 kVA |
| | | Output current (continuous) | 13 A |
| | | Maximum current | 20.8 A |
| | | PWM switching frequency | 10 kHz |
| | Filter | Inductance | 3.1 mH |
| | | Capacitance (star-connected) | 10 µF |
| | DC Link | Capacitance | 2610 µF |
| | DL | Average power | 2.2 kW |
| | $C_{exc}$ | Nominal power | 7.5 kvar |
| Control | DL regulators | Proportional and integral gains of $PI_1$ | 3; 10 |
| | | Proportional and integral gains of $PI_2$ | 10; 30 |
| | SC regulators | Proportional and integral gains of $PI_3$ | 5; 20 |
| | | Proportional and integral gains of $PI_4$ | 1; 10 |
| | SC control voltage limits | $V_{sc1}$, $V_{sc}$ (for $k_1$) | 148, 138 |
| | | $V_{scm}$, $V_{sc2}$ (for $k_2$) | 70, 100 |
| | | $V_{dc1}$, $V_{dc2}$ (for $k_3$) | 600, 650 |

## REFERENCES


[1] J. Martinez, M. Saidel, E. Fadigas, "Influence of non-dispatchable energy sources on the dynamic performance of MicroGrids," Electric Power Systems Research, vol. 131, pp. 96–104, 2016. doi: 10.1016/j.epsr.2015.09.008

[2] A.H. Kasem Alaboudy, H.H. Zeineldin, J.L. Kirtley Jr., "Microgrid Stability Characterization Subsequent to Fault-Triggered Islanding Incidents," IEEE Trans. on Power Delivery, vol. 27, no. 2, pp. 658–669, Apr. 2012. doi: 10.1109/TPWRD.2012.2183150

[3] S.M. Amelian and R. Hooshmand, "Small signal stability analysis of microgrids considering comprehensive load models – a sensitivity based approach," in Proc. of the Smart grid conference, 2013, pp. 143–149. doi: 10.1109/SGC.2013.6733828

[4] A. Kahrobaeian and Yasser A.-R. I. Mohamed, "Analysis and mitigation of low-frequency instabilities in autonomous medium-voltage converter-based Microgrids with dynamic loads," IEEE Trans Ind Electron, vol. 61, pp. 1643–1658, 2014. doi: 10.1109/TIE.2013.2264790

[5] A. Kahrobaeian and Yasser A.-R. I. Mohamed, "Stability Analysis and Control of MediumVoltage Micro-Grids with Dynamic Loads," in Proc. of IEEE Power & Energy Society General Meeting, 2013, pp. 1 - 5. doi: 10.1109/SGC.2013.6733828

[6] G. Diaz, C.G. Moran, J.G. Aleixandre, A. Diez, "Composite loads in stand-alone inverter-based microgrids – modeling procedure and effects on load margin," IEEE Trans Power Syst, 2010, vol. 25, pp. 894–905. doi: 10.1109/TPWRS.2009.2036360

[7] A.M. Abd-el-Motaleb and D. Hamilton, "Modelling and sensitivity analysis of isolated microgrids," Renewable and Sustainable Energy Reviews, vol. 47, 2015, pp. 416–426. doi: 10.1016/j.rser.2015.03.025

[8] A. Radwan and I. Mohamed, "Stabilization of medium-frequency modes in isolated Microgrids supplying direct online induction motor loads," IEEE Trans Smart Grid, 2014, vol. 5, pp. 358–370. doi: 10.1109/TSG.2013.2262503

[9] S. Saiprasad, N. Soni and S. Doolla, "Analysis of Motor Starting in a Weak Microgrid," in Proc. of 2014 IEEE PEDES Conference, pp. 1-5. doi: 10.1109/PEDES.2014.7042127

[10] M. Falahi, K.L. Butler-Purry and M. Ehsani, "Induction Motor Starting in Islanded Microgrids," IEEE Trans. on Smart Grid, Vol. 4, 2013, pp. 1323-1331. doi: 10.1109/TSG.2013.2271261

[11] A. Tazay, Z. Miao and L. Fan, "Blackstart of An Induction Motor in An Autonomous Microgrid," in Proc. of 2015 IEEE PES General Meeting, pp. 1 - 5. doi: 10.1109/PESGM.2015.7286614

[12] H.R. Baghaee, M. Mirsalim, G.B. Gharehpetian, "Performance Improvement of Multi-DER Microgrid for Small- and Large-Signal Disturbances and Nonlinear Loads: Novel Complementary Control Loop and Fuzzy Controller in a Hierarchical Droop-Based Control Scheme," IEEE Systems Journal, 2016, vol. PP, Issue: 99, pp. 1-8. doi: 10.1109/JSYST.2016.2580617

[13] I.N. Moghaddam, Z. Salami, L. Easter, "Sensitivity Analysis of an Excitation System in Order to Simplify and Validate Dynamic Model Utilizing Plant Test Data," IEEE Trans. on Industry Applications, 2015, vol. 51, pp. 3435-3441. doi: 10.1109/TIA.2015. 2406658

[14] D. M. Bui; K.-Y. Lien; S.-L. Chen, "Investigate dynamic and transient characteristics for islanded/grid-connected operation modes of microgrid and develop a Fast-Scalable-Adaptable fault protection algorithm," in Proc. of 2014 DPSP Conference on, pp. 1 – 6. doi: 10.1049/cp.2014.0061

[15] J. G. Priolkar; S. Doolla, "Analysis of PV-hydro isolated power systems", in Proc. of the 2013 Annual IEEE India Conference (INDICON), pp. 1 – 6. doi : 10.1109/INDCON.2013.6725890

[16] Y. Ren, S. Li, L. Jiang, P. Zeng, "Coordinated control for battery and supercapacitor in hybrid energy storage system in Microgrid," in Proc. of the 2016 IPEMC-ECCE Conference, pp. 2654 –2660. doi: 10.1109/IPEMC.2016.7512717

[17] Y. Yuan, C. Sun, M. Li, S.S. Choi, Q. Li, "Determination of optimal supercapacitor-lead-acid battery energy storage capacity for smoothing wind power using empirical mode decomposition and neural network," Electric Power Systems Research, 2015, vol. 127, pp. 323–331. doi: 10.1016/j.epsr.2015.06.015

[18] M. Farhadi, O. Mohammed, "Adaptive Energy Management in Redundant Hybrid DC Microgrid for Pulse Load Mitigation," IEEE Transactions on Smart Grid, 2015, vol. 6, pp. 54-62. doi: 10.1109/ TSG.2014.2347253

[19] S. Mishra, R.K. Sharma, "Dynamic power management of PV based islanded microgrid using hybrid energy storage," in Proc. of 6th International Conference on Power Systems, 2016, pp. 1-6. doi: 10.1109/ICPES.2016.7584231

[20] X. Zhao, Y.W. Li, H. Tian, H. Wu, "Energy Management Strategy of Multiple Supercapacitors in a DC Microgrid Using Adaptive Virtual Impedance," IEEE Journal of Emerging and Selected Topics in Power Electronics, 2016, vol. 4, pp. 1174-1185. doi: 10.1109/JESTPE. 2016.2601097

[21] C. Yin, M. Sechilariu, F. Locment, "Diesel generator slow start-up compensation by supercapacitor for DC microgrid power balancing," in Proc. of ENERGYCON 2016 Conference, pp. 1–6. doi: 10.1109/ENERGYCON.2016.7514058

[22] Y. Zhang, Y.W. Li, "Energy Management Strategy for Supercapacitor in Droop-Controlled DC Microgrid Using Virtual Impedance," IEEE Trans. Power Electron, 2017, vol. 32, pp. 2704–2716. doi: 10.1109/ TPEL.2016.2571308

[23] L. Shridhar, B. Singh, C.S. Jha, B.P. Singh, "Analysis of self excited induction generator feeding induction motor," IEEE Trans. on Energy Conversion, 1994, vol. 9, pp. 390-396. doi: 10.1109/ 60.300132

[24] L. Wang and C.H. Lee, "Dynamic analyses of parallel operated self-excited induction generators feeding an induction motor load," IEEE Trans on Energy Conversion, 1999, vol. 14, Issue: 3, pp. 479-485. doi: 10.1109/60.790900

[25] L. Wang and C.H. Lee, "Long shunt and short shunt connections on dynamic performance of a SEIG feeding an induction motor load," IEEE Trans Energy Convers, 2000, vol. 15( 1), pp.1–7. doi: 10.1109/ 60.849108

[26] S.P. Singh, S.K. Jain, J. Sharma, "Voltage Regulation Optimization of Compensated Self-Excited Induction Generator with Dynamic Load," IEEE Trans. On Energy Conversion, vol. 19 (4), 2004, pp. 724-732. doi: 10.1109/TEC.2004.827711

[27] B. Singh, M. Singh and A.K. Tandon, "Transient Performance of Series-Compensated Three-Phase Self-Excited Induction Generator Feeding Dynamic Loads," IEEE Trans. On Industry Applications, Vol. 46 (4), 2010, pp. 1271-1280. doi: 10.1109/TIA. 2010.2049556

[28] P. Aree, "Transient Performance of Self-Excited Wind-Turbine Induction Generator Under Induction Motor Load," in Proc. of 2014 IEEE Region 10 Conference TENCON, pp. 1-6. doi: 10.1109/ TENCON.2014.7021872

[29] P. Aree, "Starting Performance of Induction Motor under Isolated Self-Excited Induction Generator," in Proc. of 12th ECTI-CON Conference, 2015, pp. 1-5. doi: 10.1109/ECTICon.2015.7207046

[30] P. Aree and S. Lhaksup, "Dynamic Simulation of Self-Excited Induction Generator Feeding Motor Load Using Matlab/Simulink," in proc. of 11th International ECTI-CON Conference, 2014, pp. 1-6. doi: 10.1109/ECTICon.2014.6839863

[31] A. Abbou, H. Mahmoudi, and M. Akherraz, "Analysis of SEIG for a Wind Pumping Plant Using Induction Motor," International Journal of Electrical, Computer, Energetic, Electronic and Communication Engineering Vol:7, No:6, 2013, pp. 684-690.

[32] S.N. Mahato, S.P. Singh and M.P. Sharma, "Dynamic behavior of a single-phase self-excited induction generator using a three-phase machine feeding single-phase dynamic load," Electrical Power and Energy Systems, vol. 47, 2013, pp. 1–12. doi: 10.1016/j.ijepes. 2012.10.067

[33] B. Singh, S.S. Murthy, R.R. Chilipi, S. Madishetti, G. Bhuvaneswari, "Static synchronous compensator-variable frequency drive for voltage and frequency control of small-hydro driven self-excited induction generators system," IET Gener. Transm. Distrib., 2014, Vol. 8 (9), pp. 1528–1538. doi: 10.1049/iet-gtd.2013.0703

[34] Y.K. Chauhan, S.K. Jain and B. Singh, "Operating performance of static series compensated three-phase self-excited induction generator," Electrical Power and Energy Systems, vol. 49, 2013, pp. 137–148. doi: 10.1016/j.ijepes.2012.12.004

[35] V.C. Sekhar, K. Kant, B. Singh, "DSTATCOM supported induction generator for improving power quality," IET Renew. Power Gener., 2016, Vol. 10(4), pp. 495–503. doi: 10.1049/iet-rpg.2015.0200

[36] B. Singh, S.S. Murthy and S. Gupta, "Modelling of STATCOM Based Voltage Regulator for Self-Excited Induction Generator with Dynamic Loads," in Proc. of PEDES '06, pp. 1-6. doi: 10.1109/ PEDES.2006.344322

[37] B. Singh, S.S. Murthy, S. Gupta, "A Stand-Alone Generating System Using Self-Excited Induction Generators in the Extraction of Petroleum Products," IEEE Trans. on Industry Applications, Vol. 46 (1), 2010, pp. 94-101. doi: 10.1109/TIA.2009.2036519

[38] S. Sharma and B. Singh, "Isolated Asynchronous Generator in Wind Generation Feeding Dynamic Loads," in Proc. of 2010 IEEE IAS Annual Meeting, pp. 1-7. doi: 10.1109/IAS.2010.5615618

[39] M.A. Zeddini, R. Pusca, A. Sakly and M.F. Mimouni, "PSO-based MPPT control of wind-driven Self-Excited Induction Generator for pumping system," Renewable Energy, vol. 95, 2016, pp. 162-177. doi: 10.1016/j.renene.2016.04.008

[40] T. Ouchbel, S. Zouggar, M.L. Elhafyani, M. Seddik, F.Z. Kadda, "Power maximization of an asynchronous wind turbine with a variable speed feeding a centrifugal pump," Energy Conversion and Management, 2014, vol. 78, pp. 976–984. doi: 10.1016/j.enconman. 2013.08.063

[41] B. Singh, S.S. Murthy and S. Gupta, "Transient Analysis of Self-Excited Induction Generator With Electronic Load Controller (ELC) Supplying Static and Dynamic Loads," IEEE Trans. on Industry Appl, vol. 41 (5), 2005, pp. 1194-1204. doi: 10.1109/TIA.2005.855047

[42] C.P. Ion and C. Marinescu, "Autonomous micro hydro power plant with induction generator", Renewable Energy, 2011, Volume 36 (8), pp. 2259-2267. doi: 10.1016/j.renene.2011.01.028

[43] M.H. Andishgar, E. Gholipour, R-A. Hooshmand, "An overview of control approaches of inverter-based microgrids in islanding mode of operation," Renewable and Sustainable Energy Reviews, 2017, vol. 80, pp. 1043–1060. doi: 10.1016/j.rser.2017.05.267

[44] P.J. Grbovic, P. Delarue, P. Le Moigne, P. Bartholomeus, "Modeling and Control of the Ultracapacitor-Based Regenerative Controlled Electric Drives," IEEE Trans. on Industrial Electronics, vol. 58 (8), pp. 3471-3484, Aug. 2011. doi: 10.1109/TIE.2010.2087290

[45] H. Douglas; P. Pillay, "Sizing ultracapacitors for hybrid electric vehicles," in Proc. Of 31st IEEE IES Annual Conference pp. 6. doi: 10.1109/IECON.2005.1569143

[46] L. Sigrist, I. Egido, E.L. Miguélez, L. Rouco, "Sizing and Controller Setting of Ultracapacitors for Frequency Stability Enhancement of Small Isolated Power Systems," IEEE Trans. on Power Systems, 2015,Vol. 30(4), pp. 2130–2138. doi: 10.1109/TPWRS.2014.2356721

[47] A. Kuperman, M. Mellincovsky, C. Lerman, I. Aharon, N. Reichbach, G. Geula, R. Nakash, "Supercapacitor Sizing Based on Desired Power and Energy Performance," IEEE Trans. on Power Electronics, 2014, vol. 29 (10), pp. 5399–5405. doi: 10.1109/TPEL.2013.2292674

[48] Maxwell technologies, HC Series Ultracapacitors, https://ro.mouser.com/new/maxwell/maxwellhc/

[49] S. Golestan, J.M. Guerrero, J.C. Vasquez, "Three-Phase PLLs: A Review of Recent Advances," IEEE Trans. on Power Electronics, 2017, vol. 32, pp. 1894–1907. doi: 10.1109/TPEL.2016. 2565642

[50] Mathworks Inc, TransÉnergie Technologies Hydro-Québec, SimPowerSystems - For Use with Simulink

[51] C.P. Ion, I. Serban, "Improving the Stability of SEIG based microgrids during overloads by using supercapacitor-based storage and load-shedding," in Proc. of OPTIM 2017 Conference, pp. 1 – 6. doi: 10.1109/EEEIC.2017.7977675

[52] S.Z. Djokic, J. Desmet, G. Vanalme, J. V. Milanovic, K. Stockman, "Sensitivity of personal computers to voltage sags and short interruptions," IEEE Trans. on Power Delivery, 2005, vol. 20, pp. 375-383. doi: 10.1109/TPWRD.2004.837828